

24th International Congress of Theoretical and Applied Mechanics

Energy cascade in internal wave attractors

T. Dauxois^a, C. Brouzet^a, E. Ermanyuk^{a,b}, S. Joubaud^a, D. Le Tourneau^a, I. Sibgatullin^{a,c}

^aUniv Lyon, ENS de Lyon, Univ Claude Bernard Lyon 1, CNRS, Laboratoire de Physique, F-69342 Lyon, France

^bLavrentyev Institute of Hydrodynamics, Novosibirsk, Russia

^cFaculty of Mechanics and Mathematics, Moscow State University, Russia

Abstract

One of the important questions in the dynamics of the oceans is related to the cascade of mechanical energy in the abyss and its contribution to mixing. Here, we propose a unique self-consistent experimental and numerical set up that models a cascade of triadic interactions transferring energy from large-scale monochromatic input to multi-scale internal wave motion. We show how this set-up can be used to tackle the open question of studying internal wave turbulence in a laboratory, by providing, for the first time, explicit evidence of a wave turbulence framework for internal waves. Finally, beyond this regime, we highlight a clear transition to a cascade of small-scale overturning events which induce mixing.

© 2017 The Authors. Published by Elsevier B.V. This is an open access article under the CC BY-NC-ND license

(<http://creativecommons.org/licenses/by-nc-nd/4.0/>).

Peer-review under responsibility of organizing committee of the 24th International Congress of Theoretical and Applied Mechanics

Keywords: Internal waves; Stratified flows; Flow instabilities; Wave turbulence.

PACS: 47.35.Bb; PACS 47.55.Hd; PACS 92.05.Bc; PACS 47.20.-k;

1. Introduction

The continuous energy input to the ocean interior comes from the interaction of global tides with the bottom topography yielding a global rate of energy conversion to internal tides of the order of 1TW. The subsequent mechanical energy cascade to small-scale internal-wave motion and mixing is a subject of active debate in view of the important role played by abyssal mixing in existing models of ocean dynamics. The oceanographic data support the important role of internal waves in mixing, at least locally: increased rates of diapycnal mixing are reported¹ in the bulk of abyssal regions over rough topography in contrast to regions with smooth bottom topography. A question remains: how does energy injected through internal waves at large vertical scales induce the mixing of the fluid?

Let us consider a stratified fluid with an initially constant buoyancy frequency $N = [(-g/\bar{\rho})(d\rho/dz)]^{1/2}$, where $\rho(z)$ is the density distribution over the vertical coordinate z , and g the gravity acceleration. The dispersion relation is

$$\theta = \pm \arcsin(\Omega), \quad (1)$$

* Corresponding author. Tel.: +33-47272-8142 ; fax: +33-47272-8950.

E-mail address: Thierry.Dauxois@ens-lyon.fr

where θ is the slope of the wave beam to the horizontal, and Ω (resp. $\omega = \Omega N$) the non-dimensional (resp. dimensional) frequency of oscillations. This anisotropic dispersion relation requires preservation of the slope of the internal wave beam upon reflection at a rigid boundary. In the case of a sloping boundary, this property gives a purely geometric reason for a strong variation of the width of internal wave beams (focusing or defocusing) upon reflection. Internal wave focusing provides a necessary condition for large shear and overturning, as well as shear and bottom layer instabilities at slopes.

In a confined fluid domain, focusing usually prevails, leading to a concentration of wave energy on a closed loop, the internal wave attractor². At the level of linear mechanisms, the width of the attractor branches is set by the competition between geometric focusing and viscous broadening. High concentration of energy at attractors make them prone to triadic resonance instability which sets in as the energy injected into the system increases³. Note that the particular case for which both unstable secondary waves have a frequency equal to half of the forcing frequency is of special interest in the oceanographic context where viscosity is negligible. In that case, the appropriate name is parametric subharmonic instability and abbreviated as PSI. By abuse of language, some authors have sometimes extended the use of the name PSI to cases for which secondary waves are not corresponding to half of the forcing frequency. For the sake of terminological consistency, we propose to abbreviate triadic resonance instability using the acronym TRI.

The onset of instability in this case is similar to the classic concept of triadic resonance, which is best studied for the idealized case, with monochromatic in time and space carrier wave as a basic state which feeds two secondary waves via nonlinear resonant interactions. The resonance occurs when temporal $\Omega_1 + \Omega_2 = \Omega_0$ and spatial $\vec{k}_1 + \vec{k}_2 = \vec{k}_0$ conditions are satisfied (\vec{k} is the wave vector while subscripts 0, 1 and 2 refer to the primary, and two secondary waves, respectively). In a wave attractor, the wave beams serve as a primary wave, and the resonance conditions are satisfied with good accuracy³, providing a consistent physical framework for the short-term behavior of the instability.

2. The internal wave attractor to enhance the nonlinearities

2.1. Reflection of internal waves: a focusing mechanism

The dispersion relation of internal waves is very specific and leads to a very unusual reflection on a sloping boundary that has interesting properties, central for our objective as it will be immediately clear. To be more specific, let us consider an inviscid linearly stratified fluid of constant buoyancy frequency N and a sloping boundary, tilted with an angle α with respect to the vertical, as shown in Fig. 1. Note that, if this configuration does not seem natural for the reflection of internal waves on the topography at the bottom of the ocean, it corresponds by symmetry to a case with negative values of α , but is simpler for an experimental realization.

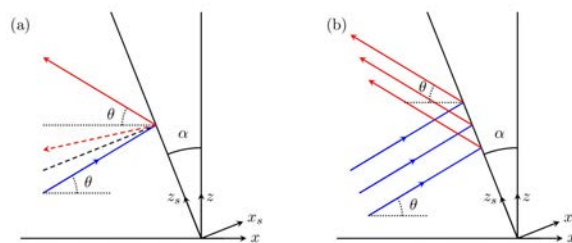


Fig. 1. (a): Reflection of an incident blue ray on the sloping boundary inclined with an angle α with respect to the vertical. In optics or acoustics, the reflected ray is the dashed red line. For internal waves, the reflected ray is the red solid line. (b): Reflection of an incident internal wave beam in blue on a sloping boundary. The reflected wave beam is in red. The slope coordinates (x_s, z_s) are shown on both panels.

As the pulsation of the wave is conserved during the reflection, both the incident and reflected waves propagate with the same angle θ , defined as $\sin \theta = \pm \Omega$. It is worth to note that this is very different from the reflection in optics or acoustics where the electromagnetic or sound waves conserve the angle with respect to the normal to the sloping boundary, referred usually as the classical Descartes reflection. For internal waves, this is the angle with the gravity

that is conserved. This difference is illustrated in Fig. 1(a). The incident ray is in blue, while the normal to the sloping boundary is represented with a dashed black line. The reflected ray for optics or acoustics is the dashed red line while the one for internal waves is the solid red line.

This non-Descartes reflection is even more intriguing, and therefore interesting, when one considers a beam, and not only a ray. This is shown in Fig. 1(b) in which the blue incident beam is reflected into the red one. The width of the reflected beam is thus reduced and one gets an energy focusing for these internal waves. It is important to emphasize that this phenomenon being a direct consequence of the linear dispersion relation, one has identified here a linear transfer toward smaller scales.

2.2. The focusing parameter

It is of course possible to get more quantitative results. The linear theory of internal wave reflection has been developed first by Phillips⁴ and is based on a well-known incident wave reflecting at a sloping boundary. Let assume that the incident wave is bi-dimensional (in the vertical plane) and can be described by the stream function

$$\psi_i(x, z, t) = \psi_{0,i} \exp \left[i \left(\omega_i t - \vec{k}_i \cdot \vec{r} \right) \right]. \tag{2}$$

The index *i* refers to the incident wave field, while ω_i and \vec{k}_i are the pulsation and wave vector of the incident wave and satisfy the dispersion relation (1). With *u* and *w* the horizontal and vertical velocity fields, the kinetic energy density is defined as

$$E_{c,i} = \frac{1}{2} (|u|^2 + |w|^2) = \frac{1}{2} (|\partial_z \psi_i|^2 + |\partial_x \psi_i|^2) = \frac{1}{2} k_i^2 |\psi_{0,i}|^2. \tag{3}$$

When the incident wave hits the sloping boundary, a reflected wave is generated and can be expressed as follows

$$\psi_r(x, z, t) = \psi_{0,r} \exp \left[i \left(\omega_r t - \vec{k}_r \cdot \vec{r} \right) \right], \tag{4}$$

where the index *r* refers to the reflected wave field. Its kinetic energy density corresponds to $E_{c,r} = \frac{1}{2} k_r^2 |\psi_{0,r}|^2$. The complete wave field is therefore $\psi = \psi_i + \psi_r$.

As the flow does not penetrate the sloping boundary, the total stream function field must vanish at the boundary defined by $x = -z \tan \alpha$. In order to simplify the boundary condition, one usually defines the coordinates attached to the slope (x_s, z_s) , as shown in Fig. 1. The velocity fields in the slope coordinate system are $(u_s, w_s) = (-\partial \psi / \partial z_s, \partial \psi / \partial x_s)$ and the wave number is noted $\vec{k}_s = (k_{x_s}, k_{z_s})$. The non-penetration condition can be expressed as $u_s = 0$ at $x_s = 0$ and for all z_s and time *t*. On the total stream function field, this becomes

$$k_{z_s,i} \psi_{0,i} \exp \left[i \left(\omega_i t - \vec{k}_{s,i} \cdot \vec{r}_s \right) \right] + k_{z_s,r} \psi_{0,r} \exp \left[i \left(\omega_r t - \vec{k}_{s,r} \cdot \vec{r}_s \right) \right] = 0, \tag{5}$$

at $x_s = 0$ and for all z_s and time *t*. This leads to $\omega_i = \omega_r \equiv \omega$, $k_{z_s,i} = k_{z_s,r}$ and $\psi_{0,i} = \psi_{0,r} \equiv \psi_0$. Thus, the frequency and the wave vector component parallel to the sloping boundary are conserved during the reflection. The normal component of the wave vector can be determined using geometrical construction and the dispersion relation: one gets $k_{x_s,i} = k_{z_s,i} \tan(\theta - \alpha)$ and $k_{x_s,r} = k_{z_s,r} \tan(\theta + \alpha)$. Thus, the ratio between the norms of the two wave vectors is given by

$$\frac{k_r}{k_i} = \left| \frac{\cos(\theta - \alpha)}{\cos(\theta + \alpha)} \right| \equiv \gamma. \tag{6}$$

This defines the focusing parameter γ . One realizes immediately that there is neither focusing, nor defocusing when the wall is vertical ($\alpha = 0$) or horizontal ($\alpha = \pi$): both cases lead indeed to $\gamma=1$. One recovers indeed the case of the Descartes reflection, since keeping the angle with respect to the gravity for the internal waves, does correspond to keep the angle with respect to the normal of the wall (that is orthogonal to the gravity!).

However as soon as one considers a sloping boundary ($\alpha \neq 0$), the focusing parameter is different from unity: it is for example greater than 1 in Fig. 1. The width of the reflected beam is thus reduced by the factor γ . This is a focusing reflection, the energy in the incident beam being concentrated into the red one. Indeed, Eq. (6) leads to $E_{c,r} = \gamma^2 E_{c,i}$ showing that the energy density is increased by a factor $\gamma^2 > 1$. It is important to realize that one can also have a defocusing reflection if the incident beam is the red one in Fig. 1(b) while the reflected beam is the blue one.

Interestingly, this parameter diverges when $\theta + \gamma$ tends to 90° . This corresponds to the case where the waves have a propagation angle very close to the slope of the boundary. This situation is called critical reflection. Indeed, it is critical because γ diverges and thus, the wave length of the reflected wave tends to 0: nonlinear and dissipation effects cannot be overlooked and should be treated carefully. Using a weakly nonlinear theory, it has been shown⁵ how to heal this singularity using matched asymptotic expansion. This is however not the case under study in the remainder of the paper.

2.3. An internal wave billiard

If one considers now a closed basin, one realizes that the above focusing mechanism will lead to an extremely efficient focusing phenomenon. After the first reflection on the sloping wall, the red beam depicted in Fig. 1(b) will reflect on the surface, then on the left vertical wall, and then on the bottom horizontal surface. These three Descartes-like reflections ($\alpha = 0$ or π) do not change neither the energy density nor the norms of the two wave vectors. However the following reflection on the sloping wall will again reduce the beam by a similar factor: it is straightforward to understand that after a few loops the beam will be extremely narrow, and indeed its width will inevitably vanishes in the limit of infinitely many reflections, leading to a single ray bouncing on the walls.

Internal wave ray tracing in different closed basin shapes has been essentially studied by Leo Maas over the last past twenty years. This can be viewed as an internal wave billiard⁶. The classical billiard studies the trajectories in a closed domain of a particle reflecting elastically and following the standard Descartes reflection. It can exhibit periodic motion, motion along an invariant curve or chaos⁷.

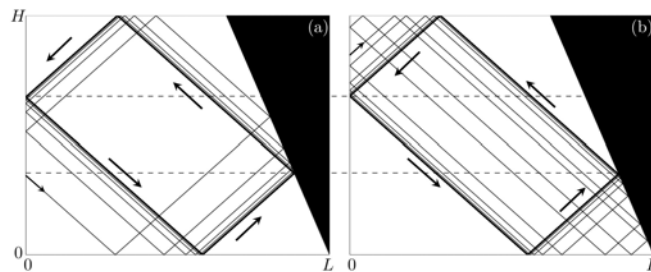


Fig. 2. Convergence towards the same attractor of two rays starting from two different points in the same geometry. The small arrows on the left vertical wall indicate the two positions where the rays start, while the large arrows show the direction of propagation of the periodic ray on the attractor. The two horizontal dashed lines shows that the two attractors reached are exactly identical.

In a trapezoidal domain, different attractors have been identified and carefully studied². They are labelled using two indices: the number of reflections at the surface (or at the bottom) and the number of reflections on the vertical side wall (or on the slope). Fig. 2 presents an attractor with only one reflection on the surface and on the vertical wall: a (1,1) attractor as the one we will use in the remainder of the paper.

However, the internal attractor is not at the goal of our study, but rather the tool to drive strong instabilities within the fluid. As we have understood from the above discussion, already within the linear regime, such a wave attractor has an extremely efficient focusing power and nonlinearity will come into play, leading to triadic resonance instabilities that will drive efficiently the wave turbulence.

2.4. Set-up

The experimental set-up used in the present work and sketched in Fig. 3 is similar to the one described previously in the literature^{3,8}. Experiments are conducted in the rectangular test tank of size $80 \times 17 \times 42.5$ cm³ filled with uniformly stratified fluid using the conventional double-bucket technique. Salt is used as a stratifying agent. The density profile is measured prior and after experiments by a conductivity probe attached to a vertical traverse mechanism. The value of the buoyancy frequency N is evaluated from the measured density profile. The trapezoidal fluid domain of length L (measured along the bottom) and depth H is delimited by a sliding sloping wall, inclined at the angle α . The wall is

slowly inserted into the fluid after the end of the filling procedure. The input forcing is introduced into the system by an internal wave generator^{9,10}. The time-dependent vertical profile of the generator is prescribed in the form

$$\zeta(z, t) = a \sin(\omega_0 t) \cos(\pi z/H),$$

where a and ω_0 are the amplitude and frequency of oscillations, respectively. In a horizontally semi-infinite domain, the motion of the generator would generate the first vertical mode of internal waves. The profile is reproduced in discrete form by the horizontal motion of a stack of 47 plates. The whole-field velocity measurements are performed via the standard PIV technique. The fluid is seeded with light-reflecting hollow glass spheres of size $8 \mu\text{m}$ and density 1100 kg/m^3 . The sedimentation velocity of particles is found to be very low, with negligible effect on results of velocity measurements. The longitudinal ($x, y = 0, z$) mid-plane of the test section is illuminated by a vertical laser sheet coming through the side of the tank. The mesh of measurements is found to be sufficient to resolve the small-scale details of the wave field. The PIV acquisition leads to 2 velocity fields per second. This sampling rate is also found to provide a sufficient resolution of the significant frequency components of the signal. For the numerical simulations, high-order spectral-element approach and modified open code nek5000 were used.

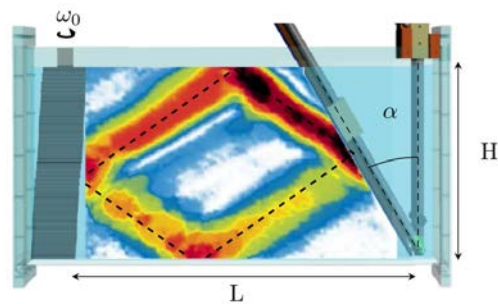


Fig. 3. *Experimental set-up.* The wave generator is on the left and the inclined slope on the right. The color inset is a typical PIV snapshot showing the magnitude of the experimental two-dimensional velocity field obtained after 15 periods $T_0 = 2\pi/(N\Omega_0)$. Black dashed lines show the billiard geometric prediction of the attractor.

3. The energy cascade revealed by the time-frequency diagram and the bicoherence plot

Using laboratory experiments and numerical simulations, we have shown that the internal wave attractor set-up, sketched in Fig. 3, provides an excellent energy cascade, emphasizing how internal wave attractors can be a novel laboratory model of a natural cascade¹¹.

Indeed, the internal wave attractor is the first step: the focalisation mechanism enhances the development of the triadic instability within the beams of the attractor. While the attractor is still visible, branches are progressively deformed by triadic resonance instability, leading to the presence of secondary waves. Once the instability is well-developed, secondary waves are acting as primary waves for higher-order triadic interactions. If the focalisation is strong enough, this mechanism will of course repeat through the instability of the secondary waves. This is what is revealed by the time frequency diagram shown in Fig. 4(a). Initially, only a signal around $\Omega_0 = 0.61$ is present, but almost immediately one distinguishes two secondary waves $\Omega_1 = 0.36$ and $\Omega_2 = 0.25$ whose sum gives Ω_0 . However, again Ω_1 and Ω_2 are destabilized and this mechanism is pursued.

To detect the frequency triplets, we use the bispectrum analysis which measures the extent of statistical dependence among three spectral components ($\Omega_k, \Omega_i, \Omega_j$) satisfying the relationship $\Omega_k = \Omega_i + \Omega_j$, with the quantity $M(\Omega_i, \Omega_j) = F(\Omega_i)F(\Omega_j)F^*(\Omega_i + \Omega_j)$, where F is the Fourier transform and $*$ denotes the complex conjugate. In practice, the bispectrum is usually normalized and considered in form of bicoherence which is 0 for triplets with random phases and 1 for triplets with perfect phase coupling. The bicoherence is shown in Fig. 4(b). In addition to the strong peak $(0.61, 0.61)$ corresponding to the forcing frequency (therefore to self-correlation), the possible triplets satisfying the

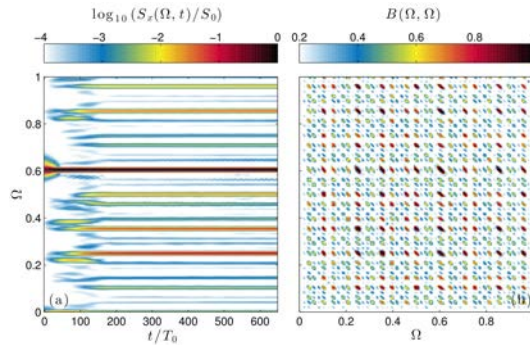


Fig. 4. Cascade of Triadic Resonance Instabilities (TRI). Time-frequency diagram (a) and its associated bicoherence (b) of the PIV signal measures in the entire trapezoidal domain.

definition of triadic resonance at $\Omega_k = \Omega_0$ can be found on the line with slope -1 connecting the points $(0, 0.61)$ and $(0.61, 0)$. This emphasizes that the mechanism at play is triadic. Other peaks are also visible corresponding to other choices of Ω_k revealing that the instability mechanism is repeated and leads to a cascade.

Thanks to this beautiful representation, it can therefore be attested that the energy transfer from global to small scales in attractors operates via a hierarchy of triadic interactions producing a complex internal wave field with a rich multi-peak discrete frequency spectrum embedded in a continuous spectrum of weaker magnitude.

4. A route towards wave turbulence

It is important to emphasize that the final stage is non-trivial since these phenomena are beyond the domain of pure wave-wave interactions: it corresponds to a regime usually called wave turbulence¹². A similar situation takes place for surface waves, where the flourishing literature gives a fully consistent description of energy cascades between components of wave spectra, only in the case of weakly nonlinear processes, while experimental reality deals with cascades significantly “contaminated” by effects of a finite size fluid domain, wave breaking, wave cusps, nonlinear dispersion, viscous damping of wave-field components, etc. The very specific dispersion relation for internal waves introduces additional complications. For instance, in rotating fluids, which have a dispersion relation analogous to stratified fluids, the usefulness of the formalism of wave turbulence as a basis for the studies in rotating turbulence has been reported for experiments only recently¹³. For internal waves, the question is still fully open, from both experimental and numerical points of view.

The presence of wave turbulence-like phenomena is illustrated in Fig. 5 using the energy spectra experimentally obtained for large scales as a diagnostic tool¹³. Horizontal and vertical velocity fields $u(x, z, t)$ and $w(x, z, t)$ are obtained with 2D PIV measurements in the entire trapezoidal domain. A two dimensions for space and one for time Fourier transform of these fields leads to $\hat{u}(k_x, k_z, \Omega)$ and $\hat{w}(k_x, k_z, \Omega)$. One can thus define the 2D energy spectrum by

$$E(k_x, k_z, \Omega) = \frac{|\hat{u}(k_x, k_z, \Omega)|^2 + |\hat{w}(k_x, k_z, \Omega)|^2}{2ST}, \tag{7}$$

where S is the area of the PIV measurement and T its duration.

In the dispersion relation for internal waves, $\Omega = \pm \sin \theta$, the wave vector \vec{k} and its components do not appear directly but they are linked with the angle θ by $\sin \theta = \pm k_x / \sqrt{k_x^2 + k_z^2}$. To compute the energy spectrum as a function of variable θ , one can interpolate the energy spectrum $E(k_x, k_z, \Omega)$ to get $E(k, \theta, \Omega)$, where k is the norm of the wave vector. For this interpolation, we define Δk as the smallest wave vector that has data points in the Cartesian coordinates. Then, one can integrate over the entire range of wave vectors $[k_{min}, k_{max}]$ as follows

$$E(\theta, \Omega) = \int_{k_{min}}^{k_{max}} E(k, \theta, \Omega) k dk, \tag{8}$$

or on any range of wave vectors between k_{min} and k_{max} . This is what has been done in Fig. 5 and the integration range represents 84% of the energy in the entire range $[k_{min}, k_{max}]$. The linear dispersion relation is seen to attract the maxima of the energy spectra. Above results are convincing signatures of a discrete wave turbulence framework for internal waves in this intermediate forcing amplitude regime.

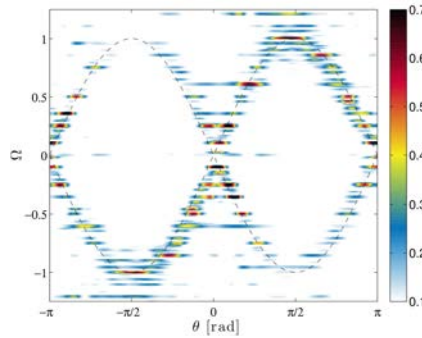


Fig. 5. Energy spectra. Colors indicate the levels of energy spectra. The black dashed lines correspond to the dispersion relation $\Omega = \pm \sin \theta = \pm k_x / \sqrt{k_x^2 + k_z^2}$. Integration across different wavenumbers ranges from 0.22 to 1 rad·cm⁻¹, i.e. wave lengths 28.5 cm to 6.3 cm.

If we repeat the same experiment with a larger amplitude, we have indications that the system is beyond the wave turbulence-like regime and has reached a mixing regime. Indeed, short-scale perturbations in particular clearly escape any relation to linear wave dynamics. This is expected to be due to overturnings, natural precursors to mixing.

5. Mixing inferred from vorticity distribution

An important issue is whether or not sufficiently energetic internal wave motion can produce an irreversible energy contribution to mixing. Fig. 6(a) presents the comparison between density profiles measured before and after experiments: while no modification of the density (within experimental error) can be observed for the intermediate amplitude forcing that leads to wave turbulence regime described in the previous section, one gets a clear evidence of mixing in case of a larger forcing amplitude.

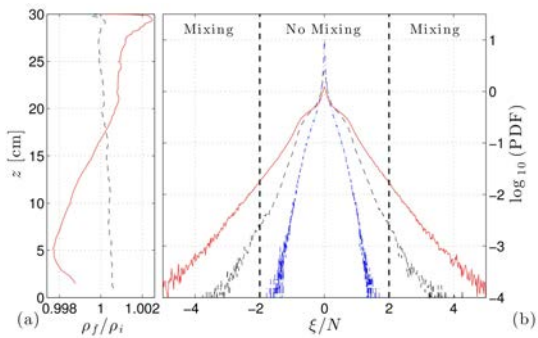


Fig. 6. Mixing and vorticity. (a) Ratio between the density profiles measured after and before the experiments for cases with intermediate (black) and large (red) forcing amplitudes. (b) Experimental probability density functions of the vorticity, calculated on the grid from experimental images for low (blue), intermediate (black) and large (red) forcing amplitudes. Figs. 4 and 5 correspond to the intermediate forcing amplitude.

Further, differences between the regimes corresponding to low and high mixing are clearly seen in statistics of extreme events. This statistics is obtained by the calculation of probability density functions (PDF). Since we are interested in small-scale events destabilizing the stratification, we take the horizontal y-component of vorticity

$\xi(x, z, t) = \partial u / \partial z - \partial w / \partial x$ measured in the vertical midplane of the test tank as a relevant quantity and consider the PDF of the dimensionless quantity ξ/N . In Fig. 6(b), we present the vorticity PDFs corresponding to different wave regimes in the attractor. In a stable attractor (see blue curve), extreme events are completely absent and the wave motion is concentrated within the relatively narrow branches of the attractor while the rest of the fluid is quiescent. Accordingly, the PDF has a sharp peak at zero vorticity and is fully localized between well-defined maximum and minimum values of vorticity. For larger forcing amplitudes (black and red curves), the development of TRI increases the probability of extreme events due to summation of primary and secondary wave components.

The occurrence of local overturning events can be viewed as a competition between stratification and vorticity. In a two-dimensional flow, a relevant stability parameter is a version of the Richardson number, which can be introduced as $Ri_\xi = N^2/\xi^2$. For a horizontal stratified shear flow this parameter reduces to the conventional gradient Richardson number $Ri = N^2/(du/dz)^2$, where du/dz is the velocity shear. Flows with large Ri are generally stable, and the turbulence is suppressed by the stratification. The classic Miles-Howard necessary condition for instability requires that $Ri < 1/4$ somewhere in the flow. If this condition is satisfied, the destabilizing effect of shear overcomes the effect of stratification, and some mixing occurs as a result of overturning. The threshold value $|\xi/N| = 2$ is marked on the plot of vorticity PDFs. It can be seen that data corresponding to large forcing amplitudes have "tails" extending into the domains $|\xi/N| > 2$. The area under the tails represents the probability of event of strength $|\xi/N| > 2$. In the larger forcing case (red curve), this probability is an order of magnitude greater than in intermediate one (blue curve), in qualitative agreement with the much higher mixing that has been reported.

6. Conclusion

We report and describe a novel experimental and numerical set up, an "internal wave mixing box", which presents a complete cascade of triadic interactions transferring energy from large-scale monochromatic input to multi-scale internal wave motion, and subsequent cascade to mixing. We report interesting signatures of discrete wave turbulence in a stratified idealized fluid problem. Moreover, we show how statistics of extreme vorticity events leads to mixing that occurs in the bulk of the fluid.

Acknowledgements

This work was supported by the LABEX iMUST (ANR-10-LABX-0064) of Université de Lyon, within the program "Investissements d'Avenir" (ANR-11-IDEX-0007) operated by the French National Research Agency (ANR). This work has achieved thanks to the resources of PSMN from ENS de Lyon.

References

1. Polzin KL, Toole JM, Ledwell JR, Schmitt RW. Spatial Variability of Turbulent Mixing in the Abyssal Ocean. *Science* 1997; **276(5309)**: 93–96.
2. Maas LRM, Benielli D, Sommeria J, Lam FPA. Observations of an internal wave attractor in a confined stably stratified fluid. *Nature* 1997; **388**:557–561.
3. Scolan H, Ermanyuk EV, Dauxois T, Nonlinear fate of internal waves attractors. *Physical Review Letters* 2013; **110**, 234501.
4. Phillips OM. *The Dynamics of the Upper Ocean*. New York: Cambridge University Press; 1966.
5. Dauxois T, Young WR. Near-critical refraction of internal waves. *Journal of Fluid Mechanics* 1999; **390**: 271–295.
6. Maas LRM, Lam FPA. Geometric focusing of internal waves. *Journal of Fluid Mechanics* 1995; **300**: 1–41.
7. Berry, MV. Regularity and chaos in classical mechanics, illustrated by three deformations of a circular billiard. *European Journal of Physics* 1981; **2**:91–102.
8. Brouzet C, Sibgatullin I, Scolan H, Ermanyuk EV, Dauxois T. Internal wave attractors examined using laboratory experiments and 3D numerical simulations. *Journal of Fluid Mechanics* 2016; **793**:109–131.
9. Gostiaux L, Didelle H, Mercier S, Dauxois T. A novel internal waves generator. *Experiments in Fluids* 2007; **42(1)**: 123–130.
10. Mercier MJ, Martinand D, Mathur M, Gostiaux L, Peacock T, Dauxois T. New wave generation. *Journal of Fluid Mechanics* 2010; **657**: 308–334.
11. Brouzet C, Ermanyuk EV, Joubaud S, Sibgatullin I, Dauxois T. Energy cascade in internal wave attractors. *Europhysics Letters* 2016; **113**:44001.
12. Nazarenko SV. *Wave Turbulence*. Lecture Notes in Physics, Berlin: Springer; 2011.
13. Yarom E, Sharon E. Experimental observation of steady inertial wave turbulence in deep rotating flows. *Nature Physics* 2014; **10**:510–514.